

The Composition of the Solar Wind in Polar Coronal Holes

George Gloeckler · Johannes Geiss

Received: 16 January 2007 / Accepted: 9 April 2007 /
Published online: 30 May 2007
© Springer Science+Business Media B.V. 2007

Abstract The solar wind charge state and elemental compositions have been measured with the Solar Wind Ion Composition Spectrometers (SWICS) on Ulysses and ACE for a combined period of about 25 years. This most extensive data set includes all varieties of solar wind flows and extends over more than one solar cycle. With SWICS the abundances of all charge states of He, C, N, O, Ne, Mg, Si, S, Ar and Fe can be reliably determined (when averaged over sufficiently long time periods) under any solar wind flow conditions. Here we report on results of our detailed analysis of the elemental composition and ionization states of the most unbiased solar wind from the polar coronal holes during solar minimum in 1994–1996, which includes new values for the abundance S, Ca and Ar and a more accurate determination of the ^{20}Ne abundance. We find that in the solar minimum polar coronal hole solar wind the average freezing-in temperature is $\sim 1.1 \times 10^6$ K, increasing slightly with the mass of the ion. Using an extrapolation method we derive photospheric abundances from solar wind composition measurements. We suggest that our solar-wind-derived values should be used for the photospheric ratios of $\text{Ne/Fe} = 1.26 \pm 0.28$ and $\text{Ar/Fe} = 0.030 \pm 0.007$.

Keywords Sun: solar wind · Sun: elemental composition · Sun: isotopic abundance ratios

1 Introduction

The first precise measurements of the composition of noble gases in the solar wind were made using the Solar Wind Composition Experiment on the five Apollo missions to the

G. Gloeckler (✉)
Department of Oceanic, Atmospheric and Space Sciences, University of Michigan, Ann Arbor,
MI 48109-2143, USA
e-mail: gglo@umich.edu

G. Gloeckler
Department of Physics, University of Maryland, College Park, MD 20742-0001, USA

J. Geiss
International Space Science Institute, Hallerstrasse 6, 3012 Bern, Switzerland
e-mail: geiss@issibern.ch

moon starting in 1969 (Geiss et al. 1970a). The first measurements of the charge state as well as the mass and charge of solar wind ions were made with a time-of-flight (TOF) mass spectrometer (CHEM) on the AMPTE spacecraft in 1982 in the magnetosheath of the Earth (Gloeckler and Geiss 1989). Both of these observations were made in the slow in-ecliptic solar wind during short time intervals of the declining phase of solar cycle 20 and 21 respectively, close to solar maximum. With the launch in 1990 of the TOF Solar Wind Ion Composition Spectrometer (SWICS) on Ulysses (Gloeckler et al. 1992) it was finally possible to observe the solar wind and continuously measure its elemental and charge state composition with a time resolution of ~ 15 minutes for tens of years under all solar wind flow conditions. The unique solar polar orbit of Ulysses allowed for the first time high-latitudes observations of the fast polar coronal hole solar wind. Geiss et al. (1995) presented the first observations of solar wind charge states (from which the freezing-in coronal temperature was determined) and composition in the fast stream from the south polar coronal hole.

A number of reports have been published that used SWICS Ulysses and ACE data to analyze solar wind composition in a variety of solar wind flows and changing solar wind conditions, employing various analysis techniques. For example, in their comprehensive study, von Steiger et al. (2000) contrasted the solar wind composition and charge state distributions in the fast, polar coronal hole solar wind with that of the slow, in-ecliptic wind. The forward model they developed estimates charge states of various elements based on probability distributions of TOF and energy values, and is best suited for studies of the variations of the composition of the more abundant elements (He, C, O, Mg, Si and Fe) and their charge states over relatively short time periods. In this paper we use a new method described below, different from that of von Steiger et al. (2000), and apply it to determine the composition and charge states in the fast solar wind at high latitude during a ~ 3 year time period starting at the end of 1993.

2 Instrumentation and Data Analysis Technique

The Solar Wind Ion Composition Spectrometer (SWICS) launched on Ulysses in 1990 uses a combination of energy per charge (ε), post-acceleration (V), followed by a time-of-flight (τ) and energy measurement (E) to determine the speed (u), mass (m) and charge (q) of solar wind and suprathermal ions with energies between 0.6 to 60 keV/charge (see Gloeckler et al. 1992 for a full description of the SWICS instrument). It then follows that $m = 2(E/\alpha) \cdot (\tau/d)^2$, $q = (E/\alpha)/(V + \varepsilon)$ and $u = (2\varepsilon \cdot q/m)^{1/2}$, where d is the time-of-flight distance (~ 10 cm) and $\alpha(m, E)$ is the energy defect, the fraction of the total energy of the ion that a solid-state detector measures. For solar wind energies, $q \approx (E/\alpha)/V$ and $m/q \approx 2V \cdot (\tau/d)^2$. Using this technique, the background noise is extremely low due to the triple coincidence measurements.

First, we accumulate a mass (m) versus mass/charge (m/q) matrix (Fig. 1), where m and m/q are calculated from measured (τ, E) pulse-height pairs using preflight calibrations of $\alpha(m, E)$, and select our data such that u is within a few percent of the simultaneously measured solar wind bulk speed, V_{SW} . For the present study we further selected data when V_{SW} was between 700 and 800 km/s. The rest of our analysis is performed using the $m - m/q$ matrix data accumulated over a three year time period and selected according to the criteria just described.

We construct a mass histogram (Fig. 2) for some selected m/q value (e.g. 2.370 ± 0.036 , blue stripe in Fig. 1). Using the least squares method, we then find best fits to the most

Fig. 1 Typical mass – mass/charge ($m - m/q$) matrix derived from measured time-of-flight and energy pulse-height signal pairs using preflight calibrations of the energy defect. (See text)

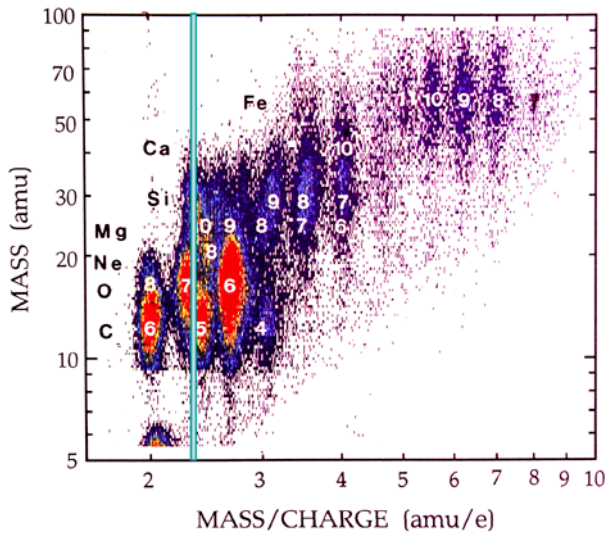


Fig. 2 Mass histogram for $m/q = 2.370 \pm 0.036$ showing the most prominent element, C, and contributions from four other elements (N, Ne, Mg and O)

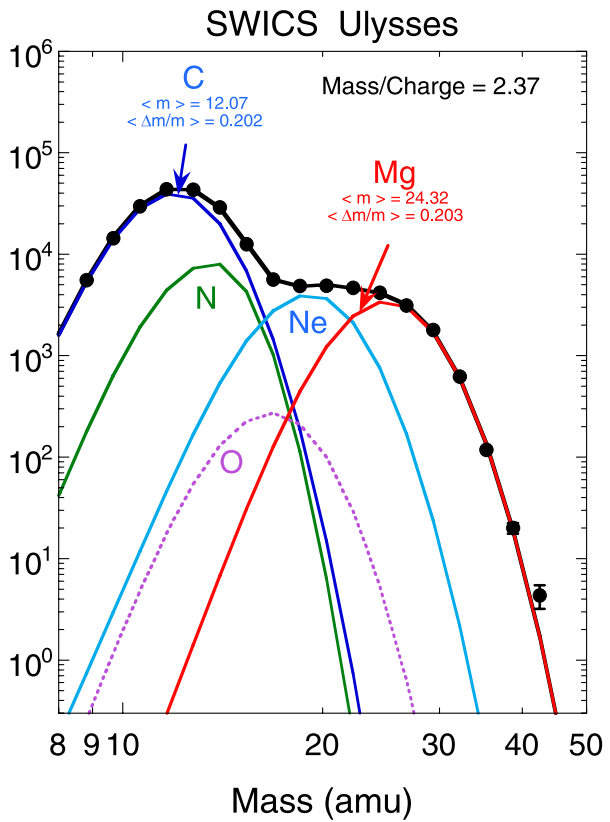
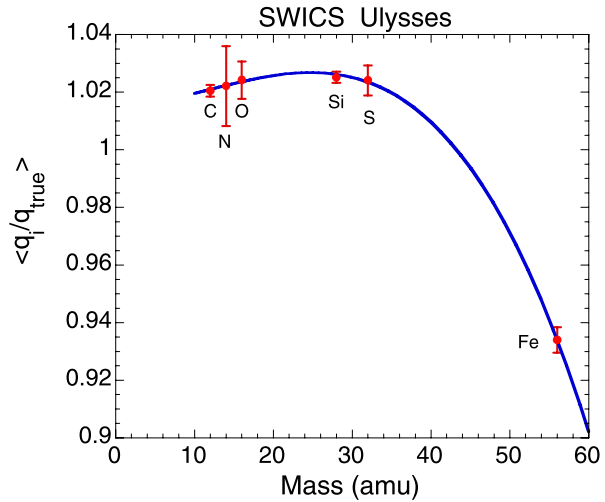


Fig. 3 Ratio of the derived to the true charge state, $\langle q_j \rangle / q_{\text{true}}$, for C, N, O, Si, S and Fe. The curve is a polynomial fit to the five values with the least uncertainties



prominent peaks (i.e. C and Mg in Fig. 2) with Gaussian distributions for each of the individual elements, j , where each distribution is characterized by c_j (integrated counts), $\langle m_j \rangle$ (mean mass) and $\langle (\Delta m/m)_j \rangle$ (width).

We repeat this procedure for all other mass histograms at different m/q values, k , and obtain c_{jk} , $\langle m_{jk} \rangle$ and $\langle (\Delta m/m)_{jk} \rangle$ for as many of elements and from as many mass histograms as possible. Finally, we find the best estimates for the ratio of the derived to the true charge state of element j $\langle q_j \rangle / q_{\text{true}} = (1/k) \cdot \sum q_{jk} / q_{\text{true}}$, where $q_{jk} = \langle m_{jk} \rangle / (m/q)_k$. Plotting $\langle q_j \rangle / q_{\text{true}}$ versus j , or equivalent mass m , as shown in Fig. 3, and fitting a polynomial curve to the best determined $\langle q_j \rangle / q_{\text{true}}$ values (i.e. C, O, Si, S and Fe) allows us to obtain from the polynomial fit estimates of $\langle q_j \rangle / q_{\text{true}}$ (and from these $\langle m_{jk} \rangle = \langle q_j \rangle \cdot (m/q)_k$) for the other, less abundant elements such as N, Ne, Mg, Ar and Ca. A similar procedure is employed to estimate best values for $\langle (\Delta m/m)_{jk} \rangle$. We then repeat the entire sequence enough times until all values for $\langle q_j \rangle / q_{\text{true}}$ and $\langle (\Delta m/m)_{jk} \rangle$ converge.

Figures 4, 5 and 6 show mass per charge distributions of individual elements. These distributions were derived using the integrated counts (c_{jk}) obtained in the final fits from mass histograms such as those shown in Fig. 2. With this technique clear separation of individual charge states of each element is obtained, and detection of rare charge states, such as C^{3+} , N^{4+} , O^{5+} and Ne^{7+} , is possible.

3 Results

3.1 Ionization Fractions

We obtain ion fraction distributions for each element by dividing the total counts for each charge state by the detection efficiency (typically 0.4 to 0.6) of that charge state. Detection efficiencies were determined from preflight calibrations using a limited number of elements (H, He, C, N, O, Ne, Ar and Kr), and contribute most to the systematic uncertainties of our measurements. We used the efficiency model of Christina Cohen (private communication).

In Figs. 7 and 8 we show the average ion fraction distributions for ^{12}C , ^{14}N , ^{16}O , ^{20}Ne , ^{24}Mg , ^{28}Si , ^{32}S and ^{56}Fe in the 700–800 km/s high-latitude solar wind from polar coronal

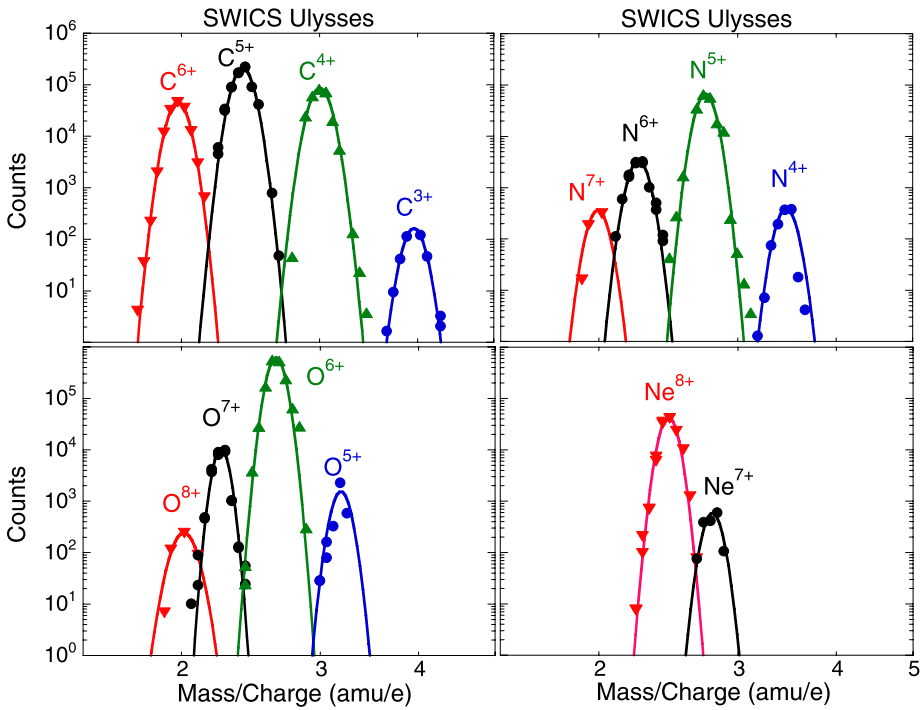
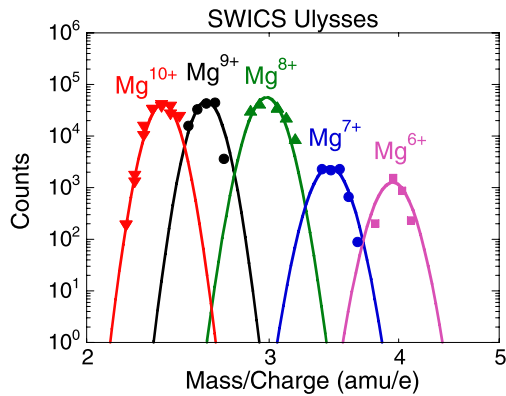


Fig. 4 Mass per charge distributions for C, N, O and Ne. Multiple data points at a given m/q value are from different estimates of integrated counts and indicate roughly the uncertainties in these estimates. Curves are Gaussian fits to the individual distributions

Fig. 5 Same as Fig. 4 but for Mg



holes during solar minimum. At this stage of our analysis we could only obtain the most dominant charge state for Ar and Ca, 8 and 10 respectively. The ion fraction distributions for all of the elements shown, except for carbon, are well described by an equilibrium charge state distribution at a single freezing-in temperature. The most probable freezing-in temperature for each element is given in each respective panel of Figs. 7 and 8 and in Table 1.

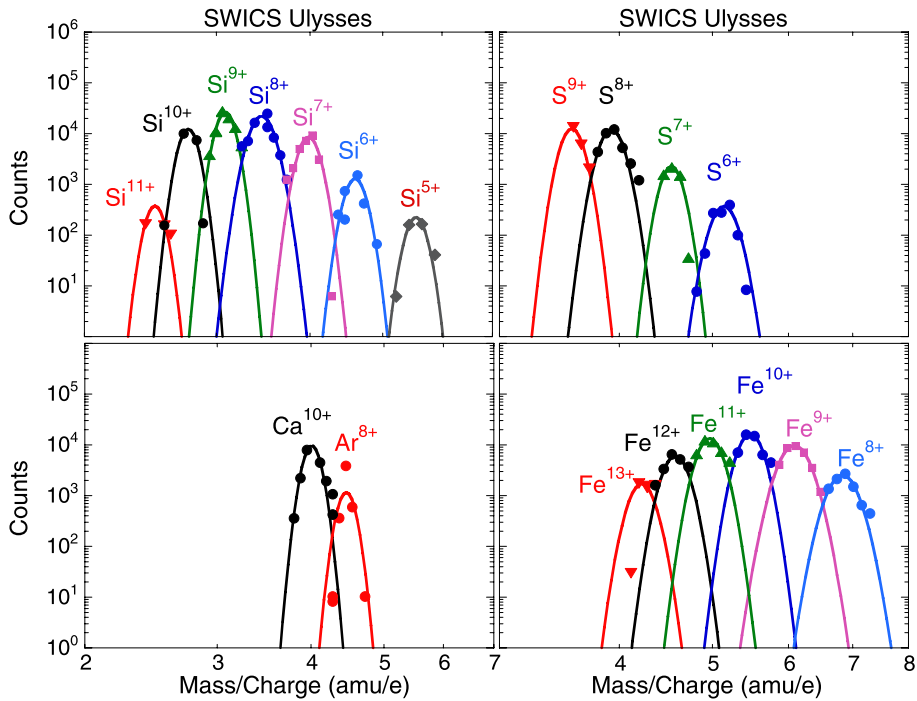


Fig. 6 Same as Fig. 4 but for Si, S, Ar, Ca and Fe

The observed ion fraction distribution for carbon is narrower than that of any of the equilibrium charge state model distributions at a single temperature. No combination of equilibrium model distributions with different temperatures can match the observed distribution. However, the wave driven, two-fluid coronal hole model of Bürgi and Geiss (1986) predicts an ion fraction distribution for carbon that fits the measured distribution extremely well, as shown in upper left-hand panel of Fig. 7. Bürgi and Geiss (1986) have shown that due to the low electron density, carbon ions depart from local equilibrium at low solar altitude and are frozen-in below the temperature maximum. Their coronal hole model also gives good fits to the observed ion fraction distributions for N, O and Ne but not for heavier elements, for which their model predicts a lower freezing-in temperature for higher charge states and a lower abundance of higher charge states compared to those observed. As the authors point out, this discrepancy could be eliminated, if coronal electron velocity distributions had suprathermal tails, instead of being maxwellian as they assumed, and/or if differential velocities between charge states played an important role.

The freezing-in temperatures and errors are listed in the last column of Table 1. The dependence on ion mass of the freezing-in temperature, T , of C, N, O, Ne, Mg, Si, S and Fe are shown in Fig. 9. The average freezing-in temperature is 1.09×10^6 K and appears to increase slightly with increasing mass, a trend also seen in the results of the coronal hole model of Bürgi and Geiss (1986). Fitting a power law to our best-determined temperatures (O, Si, S and Fe), we find that $T = 0.84M^{0.084}$. We point out that the freezing-in temperature of nitrogen is well below that of the other ions. While at this stage of our analysis we could only determine the abundance of a single charge state of Ar and Ca respectively, the identified charge states are compatible with a freezing-in temperature of $\sim 10^6$ K.

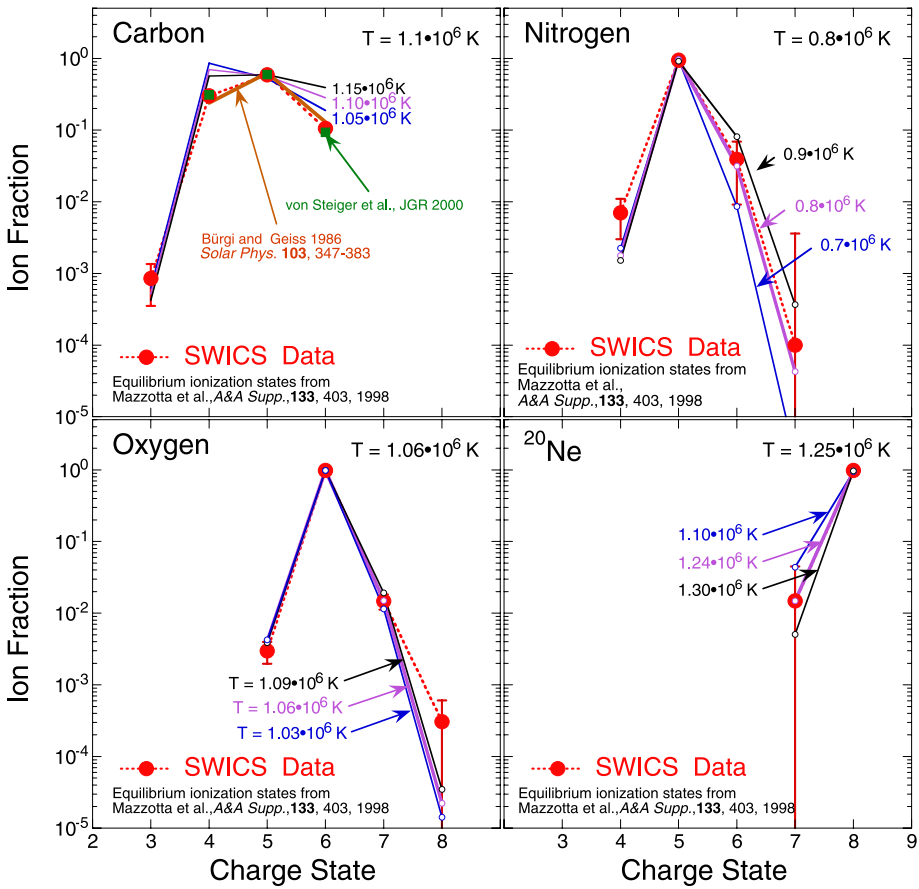


Fig. 7 Ion fraction distributions for ^{12}C , ^{14}N , ^{16}O and ^{20}Ne measured in the high-speed stream solar wind from polar coronal holes during solar minimum (large red filled circles). Error bars ($1-\sigma$) include statistical and estimated systematic uncertainties. Equilibrium charge state model distributions (Mazzotta et al. 1998) for the average and $\pm 1-\sigma$ values of the freezing-in temperature are shown next to the temperature for which they are computed. For carbon, ion fraction measurements of von Steiger et al. (2000) for the polar coronal hole solar wind are indicated by filled green squares

3.2 Elemental Abundance

We obtain the elemental abundances by summing the efficiency-corrected counts for each charge state of a given element. The abundance ratios of ^{12}C , ^{14}N , ^{20}Ne , ^{24}Mg , ^{28}Si , ^{32}S , ^{36}Ar , ^{40}Ca and ^{56}Fe , relative to ^{16}O , are given in column 2 of Table 1. The errors are due mostly to the estimated systematic uncertainties of the efficiencies for detecting a given ion.

4 Discussion

We now compare the elemental abundance in the high-speed solar wind from polar coronal holes during solar minimum (Table 1, column 2) to photospheric abundance ratios (Table 1, column 3; Asplund et al. 2005). Plotted in the left-hand panel of Fig. 10 as a function of

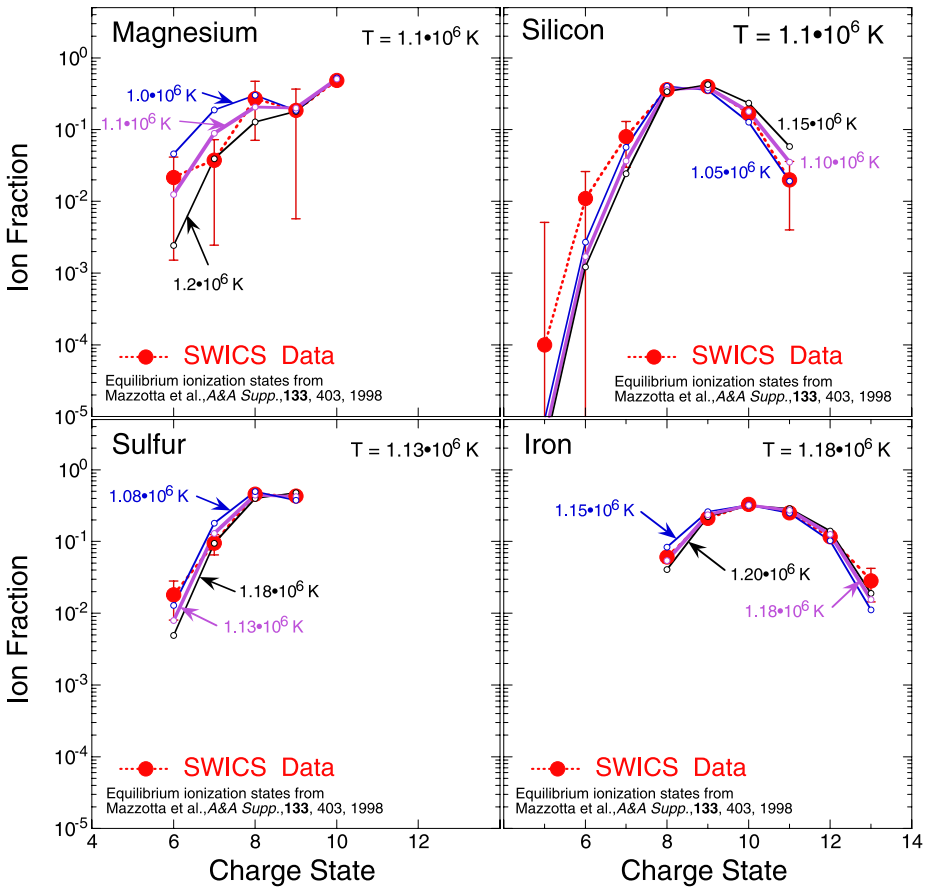


Fig. 8 Same as Fig. 7 except for Mg, Si, S and Fe

the first ionization potential (FIP) is R , the abundance ratio, relative to Fe, in the solar wind divided by the respective abundance ratio, also relative to Fe, in the photosphere. We have chosen to normalize to iron rather than to oxygen, as is usually done, because the solar wind Fe can now be measured accurately and the value of the photospheric abundance of iron has remained fairly stable for many years, unlike that of oxygen. Except for Ar and Ne, all ratios are, within uncertainties, equal to one. Neon and argon are about a factor of two below one.

In the right-hand panel of Fig. 10 we show the same solar wind to photospheric ratios, R , as in the left-hand panel but now as a function of standard ionization time (SIT), introduced by Geiss and Bochsler (1985) (see also von Steiger and Geiss 1989; Geiss 1998) as a more physical parameter than FIP. Neon and argon are a factor of two below N and O, even though all these elements have about same standard ionization time.

While composition of Ne and Ar can be measured in the corona using spectroscopic observations (e.g. Feldman and Widing 2003), the photospheric abundances of these noble gases are not available directly from spectroscopy due to lack of suitable spectral lines, and in the past have been estimated from solar energetic particle measurements (Reames 1999). We believe that a far better method to derive the abundance of Ne and Ar in the photosphere is to use solar wind measurements of Ne and Ar in both the high-speed stream

Table 1 Elemental abundances and freezing-in temperature of the high-speed solar wind from the polar coronal holes during solar minimum, and photospheric abundance ratios derived from solar wind and spectroscopic measurements

Element	Coronal hole abundance ratio ^a	Photospheric abundance ratio ^b	Photospheric abundance ratio	Freezing-in temperature (K)
¹² C	0.710 ± 0.080	0.537 ± 0.09	0.715 ± 0.09 ^c	(1.1 ± 0.08) × 10 ⁶
¹⁴ N	0.143 ± 0.016	0.132 ± 0.025	0.145 ± 0.019 ^c	(0.8 ± 0.1) × 10 ⁶
¹⁶ O	≡1.000	≡1.000	≡1.000	(1.06 ± 0.03) × 10 ⁶
²⁰ Ne	0.071 ± 0.010	[0.151 ± 0.028]	0.078 ± 0.017 ^c	(1.25 ± 0.15) × 10 ⁶
²⁴ Mg	0.108 ± 0.022	0.074 ± 0.018	0.077 ± 0.028 ^c	(1.1 ± 0.15) × 10 ⁶
²⁸ Si	0.088 ± 0.014	0.071 ± 0.011	0.066 ± 0.026 ^c	(1.1 ± 0.05) × 10 ⁶
³² S	0.035 ± 0.004	0.030 ± 0.005	0.035 ± 0.004 ^d	(1.13 ± 0.05) × 10 ⁶
³⁶ Ar	0.0018 ± 0.0004	[0.0033 ± 0.0008]	0.0018 ± 0.0004 ^d	–
⁴⁰ Ca	0.007 ± 0.003	0.0045 ± 0.0007	–	–
⁵⁶ Fe	0.067 ± 0.007	0.062 ± 0.010	–	(1.175 ± 0.025) × 10 ⁶

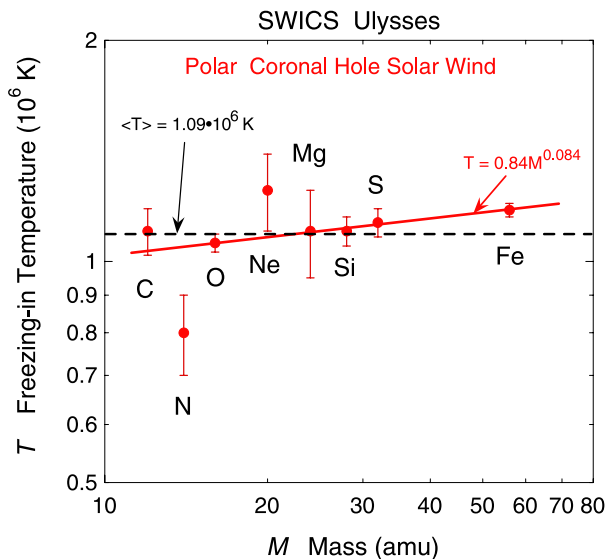
^aErrors are mostly systematic

^bFrom Asplund et al. (2005). Ne/O and Ar/O ratios based on extrapolations from solar energetic particle abundances (Reames 1999)

^cExtrapolated from solar wind measurements (see Fig. 11)

^dPolar coronal hole value from column 2

Fig. 9 Freezing-in temperature of C, N, O, Ne Mg, Si, S and Fe as a function of ion mass. Error limits are freezing-in temperatures of the ±1-σ equilibrium model fits to the ion fraction distributions of the respective ions from Figs. 7 and 8



and in the slow wind. This method was first use by Gloeckler and Geiss (2000) to determine the photospheric (or outer convective zone) abundance of ³He/⁴He (also see Fig. 6 of Gloeckler and Fisk 2007), and is illustrated in Fig. 11 for the case of Si/O and Ne/O. The photospheric values of these two ratios using this solar wind extrapolation method are listed in column 4 of Table 1 along with those of C, N, Mg, S and Ar. Except for Ne and Ar,

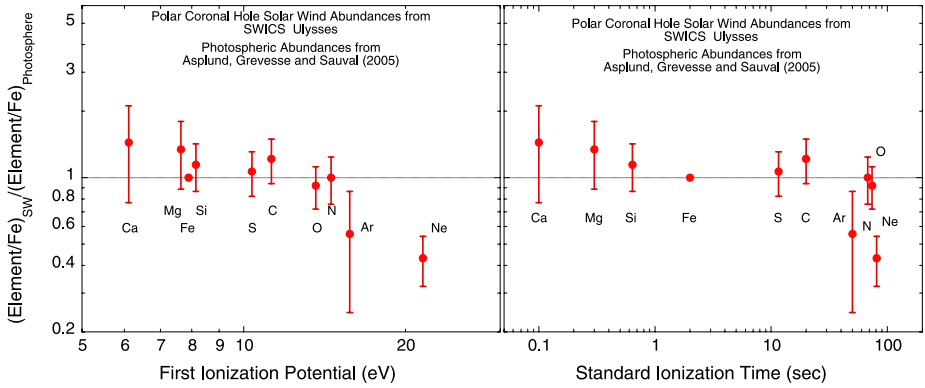
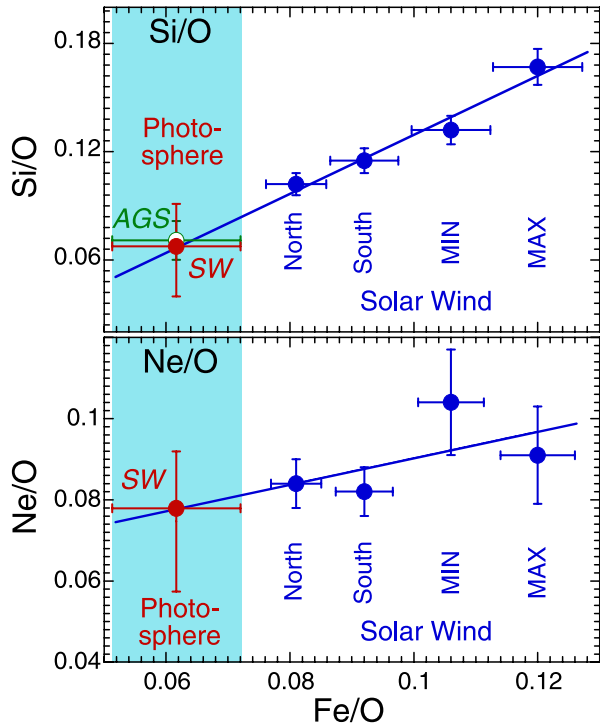


Fig. 10 R , the abundance ratio, relative to Fe, of the high-speed solar wind from polar coronal holes at solar minimum divided by the respective abundance ratio, also relative to Fe, of the photosphere, versus the first ionization potential or FIP (*left-hand panel*), and versus the standard ionization time or SIT (*right-hand panel*). Error bars include uncertainties of both the solar wind and photospheric ratios

Fig. 11 Solar wind Si/O (*top panel*) and Ne/O (*bottom panel*) abundance ratios versus Fe/O ratios measured with SWICS on Ulysses (von Steiger et al. 2000) during various solar wind flow conditions (*blue filled circles*; see von Steiger et al. 2000 for description of the four time periods: North, South, MIN and MAX). The *blue lines* represent least squares fits to the four respective solar wind data points. Extrapolation of the best-fit lines to the photospheric Fe/O abundance ratio (Asplund et al. 2005) gives an estimate of the Si/O (*top panel*) and Ne/O (*bottom panel*) abundance ratios in the photosphere (*red filled circles*). Errors of the solar wind ratios are mostly systematic and will be reduced in the future. The well-established photospheric Si/O ratio derived from spectroscopic measurements (Asplund et al. 2005) is indicated by the green *unfilled circle* labeled AGS in the *top panel*



whose photospheric abundance cannot be obtained from spectroscopic measurements, and for C, the agreement between the solar-wind-derived photospheric values (column 4) and the corresponding ratios of Asplund et al. (2005), listed in column 2 of Table 1, are quite remarkable. We therefore suggest that for the photospheric values of neon and argon our solar-wind-derived ratios, $\text{Ne}/\text{O} = 0.078 \pm 0.017$ and $\text{Ar}/\text{O} = 0.0018 \pm 0.0004$, be adopted.

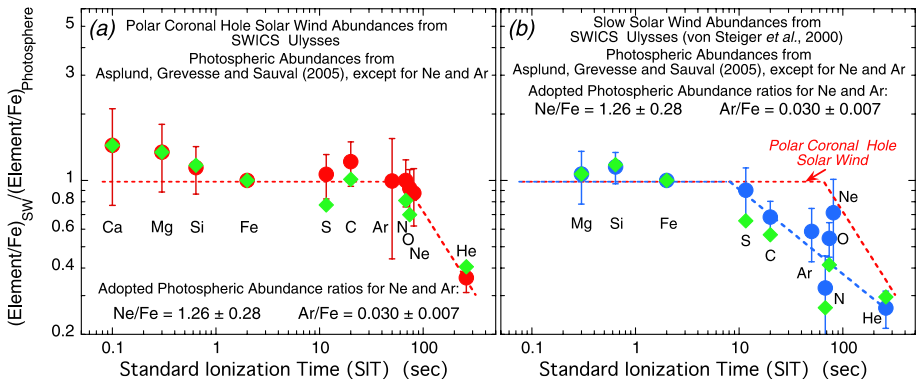


Fig. 12 (a) Same as right-hand panel of Fig. 10, but now using values of 1.26 ± 0.28 and 0.030 ± 0.007 for the photospheric abundance of Ne and Ar relative to Fe, respectively (*filled red circles*). The fast solar wind He/Fe ratio is the average of the southern and northern polar coronal hole values of von Steiger et al. (2000). (b) Same as (a), but for the slow solar wind. The solar wind abundances for all elements shown (except Ar) are the average of the MIN and MAX data of von Steiger et al. (2000). The solar wind Ar/Fe ratio is derived from the Geiss et al. (2004) Apollo $^{20}\text{Ne}/^{36}\text{Ar}$ ratio (49 ± 7) and the von Steiger et al. (2000) solar maximum (MAX) period Ne/Fe ratio of 0.76 ± 0.32 . The photospheric Ne/Fe and Ar/Fe ratios used were 1.26 ± 0.28 and 0.03 ± 0.007 , respectively. The slow solar wind He/Fe ratio is the MAX value of von Steiger et al. (2000). Date points represented by *filled green diamonds in both panels* are computed using Grevesse and Sauval (1998) photospheric abundance ratios instead of the Asplund et al. (2005) values (Ne and Ar points are not shown). With these older photospheric ratios the SIT patterns remains basically the same, but the onset of progressively reduced abundance of high-SIT elements would move to ~ 2 to 3 times lower SIT values. Our basic conclusions remain, however, unchanged

The solar wind C/O and Fe/O abundance ratios are especially well determined from SWICS measurements. It is therefore surprising that both the solar-wind-derived photospheric C/O and the measured C/O ratio in the solar minimum polar coronal solar wind are about 30% higher than the Asplund et al. (2005) C/O ratio. We hope that this discrepancy will be resolved with further improvements of models of the solar atmosphere and better efficiency models for the SWICS instruments.

In Fig. 12a we use our solar-wind-derived photospheric values for $\text{Ne/Fe} = 1.26 \pm 0.28$ and $\text{Ar/Fe} = 0.030 \pm 0.007$ (obtained by dividing the corresponding ratios in column 4 of Table 1 by the photospheric $\text{Fe/O} = 0.062$ ratio). With this adjustment the solar wind composition is, within errors, the same as the photospheric composition for all elements with standard ionization times (SIT) below ~ 70 .

The ratio R for the slow, mostly in-ecliptic solar wind as a function of SIT is shown in Fig. 12b. We used the average of the two slow solar wind (MIN and MAX) composition measurements of von Steiger et al. (2000) for C, N, O, Ne, Mg, Si, S and Fe and the Apollo Foil Experiment value for the Ar/Ne ratio (Geiss et al. 2004). For the photospheric composition we used the Asplund et al. (2005) value, except for Ne and Ar for which we used our adopted photospheric abundance of $\text{Ne/Fe} = 1.26 \pm 0.28$ and $\text{Ar/Fe} = 0.030 \pm 0.007$. It is clear that in this slow solar wind, unlike in the fast polar coronal hole solar wind, the ratios R begin to decrease from one at SIT of about 7 seconds. Thus, whatever process causes the neutral gas in the chromosphere to become ionized, it is at least an order of magnitude faster in the region of origin of the slow wind compared to polar coronal hole regions. What this process is remains an open question.

In Fig. 12 we also plotted the He/Fe ratios for both the fast and slow solar wind. In both cases this ratio is far below its photospheric value. When helium was first measured in the

solar wind (Neugebauer and Snyder 1966), the He/H ratio was found to be typically ≤ 0.04 , much lower than the expected solar ratio. The helium deficit was attributed to a lack of acceleration in the corona. Geiss et al. (1970b) derived a drag factor $\Gamma = Q^2/(2A - Q - 1)$ that governs the collisional acceleration of minor ions with Q and atomic weight A in a proton–electron plasma, and they confirmed by numerical integration that in such a two-component solar wind, momentum transfer is lower for ${}^4\text{He}^{++}$ than it is for all heavier ions up to and beyond iron. Geiss et al. (1970b) emphasized that their numerical results and their drag factor Γ neglect thermal diffusion, wave-particle interactions, and the momentum transfer of helium to the other components of the plasma in the corona and solar wind. The momentum equation integrated by F. Bürgi included these three factors, and showed that they have a major influence on the acceleration, charge state distribution and abundance of individual ion species in the solar wind (Bürgi and Geiss 1986). While the factor Γ or similar drag factors remain useful for roughly comparing the importance of coulomb drag between different ion species, numerical models are needed for quantitatively assessing ion abundances or charge state distributions.

In 1977 Bame et al. (1977) discovered that the He/H ratio in the high speed streams coming out of coronal holes is very steady at 0.048, but still considerably lower than in the outer convective zone where its value is now found to be 0.084 (Perez Hernandez and Christensen-Dalsgaard 1994). Following these observations, Geiss (1982) argued that the persistent depletion of the He/H ratio by a factor of 1.6 cannot be produced in the corona, but could result from a separation process operating below the corona at temperatures $T \approx 10^4$ K, i.e. in the chromosphere (and perhaps the transition region), that level in the solar atmosphere, where the so called FIP effect, which is the overabundance of Mg, Si and Fe relative to C, N and O, is produced. Consequently, FIP effect models that included helium were developed for chromospheric conditions (Geiss and Bochsler 1985; von Steiger and Geiss 1989). Shortly afterwards, it was discovered what nobody had predicted: The FIP effect was very much lower in the fast, coronal hole solar wind than in the slow solar wind (Gloeckler et al. 1989; von Steiger et al. 1992).

In Figs. 10 and 12 we normalize abundances to the Mg–Si–Fe plateau (we use Fe, the best determined element in this group). This normalization makes sense, because the proposed FIP mechanisms operate in competition between ionization time and a time constant (SIT) that characterizes the separation of ions from atoms. The existence of the plateau of low FIP elements implies that these elements were fully ionized at the time of separation. On the other hand, elements with FIP $> \sim 10$ eV or SIT $> \sim 10$ seconds are depleted in the slow solar wind, because they were not yet fully ionized at the time of ion–atom separation.

Our best estimates of the photospheric abundance of isotopes and those elements for which no suitable spectral lines exist now come from solar wind measurements in the slow wind and high-speed streams as illustrated in Fig. 11. Still, it would be good to underpin this empirical method by a theory of the FIP or SIT effect that explains the difference in depletion of high FIP elements, including helium, between the slow solar wind and the coronal-hole high-speed streams.

5 Conclusions

We have determined the average abundances and ion fraction distributions of ${}^{12}\text{C}$, ${}^{14}\text{N}$, ${}^{16}\text{O}$, ${}^{20}\text{Ne}$, ${}^{24}\text{Mg}$, ${}^{28}\text{Si}$, ${}^{32}\text{S}$, ${}^{36}\text{Ar}$, ${}^{40}\text{Ca}$ and ${}^{56}\text{Fe}$ in the high-speed solar wind from polar coronal holes during solar minimum using a new analysis technique. We find and conclude that:

1. Except for carbon all other elements either have, or are consistent with having, a single equilibrium freezing-in temperature.
2. The average freezing-in temperature is $\sim 1.1 \times 10^6$ K and shows a slight increase with increasing mass.
3. Carbon alone has an observed ion fraction distribution that is significantly narrower than that predicted by equilibrium charge state models at any single freezing-in temperature. Its ion fraction distribution, however, agrees well with predictions of the multi-fluid coronal hole model of Bürgi and Geiss (1986).
4. Except for He and probably Ne, the composition of the high-speed solar wind from polar coronal holes during solar minimum has no FIP effect, i.e. the elemental ratios relative to Fe, in this solar wind and in the photosphere are, within errors, the same.
5. We used an extrapolation method to derive photospheric abundances from solar wind composition measurements in various types of solar wind flows, ranging from the polar coronal hole flow at solar minimum to the solar maximum slow solar wind. These solar-wind-derived photospheric ratios are in excellent agreement (except for C) with corresponding photospheric ratios that can be obtained from spectral lines. We therefore recommend that for the best estimates of the photospheric abundance of neon and argon are our solar-wind-derived values of $\text{Ne/Fe} = 1.26 \pm 0.28$ and $\text{Ar/Fe} = 0.030 \pm 0.007$.
6. The slow solar wind, unlike the fast polar coronal hole solar wind, has a SIT effect that causes the abundance of elements in the solar wind with standard ionization times larger than about 7 sec to be below that of corresponding elements in the photosphere.
7. Whatever process causes the ionized gas in the chromosphere to separate from the neutral gas and then escape, is at least an order of magnitude faster in the region of origin of the slow solar wind than it is in polar coronal hole regions.

In our future work we will apply this technique to obtain more accurate estimates of solar wind composition and charge states using SWICS Ulysses and ACE data in a variety of solar wind flow conditions, and in particular as a function solar wind speed.

Acknowledgements This work was supported, in part, by NASA contract NAGR-10975, and by JPL contract 1237843.

References

- M. Asplund, N. Grevesse, A.J. Sauval, in *Cosmic Abundances as Records of Stellar Evolution and Nucleosynthesis in honor of David L. Lambert*, ed. by T.G. Barnes III, F.N. Bash, vol. 336 (Astronomical Society of the Pacific, 2005), p. 25
- S.J. Bame, J.R. Asbridge, W.C. Feldman, J.T. Gosling, J. Geophys. Res. **82**, 1487 (1977)
- A. Bürgi, J. Geiss, Sol. Phys. **103**, 347–383 (1986)
- U. Feldman, K.G. Widing, Space Sci. Rev. **107**, 665–720 (2003)
- J. Geiss, Space Sci. Rev. **33**, 201 (1982)
- J. Geiss, Space Sci. Rev. **85**, 241–252 (1998)
- J. Geiss, P. Bochsler, in *Proc. Rapports Isotopiques dans le Système Solaire* (Cepadues Editions, Paris, 1985), pp. 213–228
- J. Geiss, P. Eberhardt, F. Bühler, J. Meister, P. Signer, Geophys. Res. **75**, 5972–5979 (1970a)
- J. Geiss, P. Hirt, H. Leutwyler, Sol. Phys. **12**, 458 (1970b)
- J. Geiss, F. Bühler, H. Cerutti, P. Eberhardt, C.H. Filleux, J. Meister, P. Signer, Space Sci. Rev. **110**, 307–335 (2004)
- J. Geiss, G. Gloeckler, R. von Steiger, H. Balsiger, L.A. Fisk, A.B. Galvin, F.M. Ipavich, S. Livi, J.F. McKenzie, K.W. Ogilvie, B. Wilken, Science **268**, 1033–1036 (1995)
- G. Gloeckler, L.A. Fisk (2007), this volume
- G. Gloeckler, J. Geiss, in *Cosmic Abundances of Matter*, ed. by C.J. Waddington. AIP Conf. Proc., vol. 183 (1989), p. 49

- G. Gloeckler, J. Geiss, in *The Light Elements and Their Evolution*, ed. by L. Da Silva, M. Spite, J.R. De Medeiros. AIU Symposium, vol. 198 (2000), p. 224
- G. Gloeckler, J. Geiss, H. Balsiger, P. Bedini, J.C. Cain, J. Fischer et al., *Astron. Astrophys. Suppl. Ser.* **92**, 267 (1992)
- G. Gloeckler, F.M. Ipavich, D.C. Hamilton, B. Wilken, G. Kremser, *EOS Trans. AGU* **70**, 424 (1989)
- N. Grevesse, A.J. Sauval, *Space Sci. Rev.* **85**, 161–174 (1998)
- P. Mazzotta, G. Mazzitelli, S. Colafrancesco, N. Vittorio, *Astron. Astrophys. Suppl. Ser.* **133**, 403–409 (1998)
- M. Neugebauer, C.W. Snyder, *J. Geophys. Res.* **71**, 4469 (1966)
- F. Perez Hernandez, J. Christensen-Dalsgaard, *Mon. Not. Roy. Astron. Soc.* **269**, 475 (1994)
- D.V. Reames, *Space Sci. Rev.* **90**, 413 (1999)
- R. von Steiger, J. Geiss, *Astron. Astrophys.* **225**, 222–238 (1989)
- R. von Steiger, S.P. Christon, G. Gloeckler, F.M. Ipavich, *Astrophys. J.* **389**, 791–799 (1992)
- R. von Steiger, N.A. Schwadron, L.A. Fisk, J. Geiss, G. Gloeckler, S. Hefti, B. Wilken, R.F. Wimmer-Schweingruber, T.H. Zurbuchen, *J. Geophys. Res.* **105**, 27,217 (2000)